

The development of high energy X-ray total scattering method at Beijing Synchrotron Radiation Facility*

Caijuan Shi,^{1,2} Dongliang Yang,^{1,2} Lirong Zheng,¹ Yiming Yang,¹ Fei Zhang,¹ Bingbing Zhang,¹ and Xiaodong Li^{1,†}

¹Beijing Synchrotron Radiation Facility, Institute of High Energy Physics, CAS, Beijing, 100049, P R China

²These authors contributed equally: Caijuan Shi, Dongliang Yang.

As a powerful local structure probe, high energy X-ray total scattering method has been used widely in condensed matter physics, materials science and other fields. With a super-conducting wiggler (SCW) and sagittal focusing monochromator, a high energy X-ray total scattering apparatus has been developed at 3W1 beamline of Beijing Synchrotron Radiation Facility, BSRF, a first-generation synchrotron source. The total scattering apparatus mainly consists of a large two-dimensional flat-panel detector and high-energy X-rays of 50-70 keV, enabling total scattering measurements to be carried out for pair distribution function (PDF) analysis with a Q range of 0.5-25 \AA^{-1} . Based on this apparatus, a series of in-situ devices were developed, enabling the acquisition and analysis of data with a decent signal-to-noise ratio under various conditions. Demonstration results, including the observation of perovskite oxides with various A-site doping and bioactive glasses upon annealing, were presented. The practices outlined herein validated that the PDF method is capable of characterizing complex material structure at the atomic level. As synchrotron facilities continue to advance, this work stands as a critical source for fostering collaboration and driving progress in the field of scattering science.

Keywords: High energy X-ray, Total scattering, Beijing Synchrotron Radiation Facility, Pair distribution function

I. INTRODUCTION

Bragg diffraction provides experimental access to the atomic scale, revealing the average long-range order of atomic structures in crystalline materials under the assumption of lattice periodicity. However, relying solely on long-range structural information is insufficient. On the one hand, almost all crystals are imperfect, containing various inevitable defects such as point defects, dislocations, and chemical inhomogeneity [1]. Many properties of crystalline materials are profoundly influenced by these local structural disorders. On the other hand, materials with amorphous characteristics cannot be analyzed using Bragg diffraction, necessitating alternative methods to elucidate their local structures [2, 3].

A variety of local structure probes are available, including extended X-ray absorption fine structure (EXAFS) [4] nuclear magnetic resonance (NMR), Raman spectra [5, 6] and others. Among these techniques, the pair distribution function (PDF) derived from the high-energy X-ray total scattering method has garnered significant attention because of its compatibility with in-situ devices and excellent signal-to-noise ratio. The total scattering technique involves measuring the complete diffraction pattern, which encompasses both Bragg and diffuse components. This method collects data across reciprocal space, utilizing high-energy synchrotron X-rays to cover a broad range of momentum transfer (Q). From these total scattering measurements, the weighted probability of finding atoms at specific distances from other atoms, known as the PDF, can be determined.

The resolution of the PDF method is determined by the maximum value Q , Q_{\max} ($\Delta r \approx 2\pi/Q_{\max}$). Q_{\max} is limited by the wavelength of the X-ray, λ , the area of the detector, and the distance from sample to detector, since $Q = 4\pi \sin \theta / \lambda$, where 2θ is the scattering angle. It is essential to decrease λ to get larger Q_{\max} . Expect for the wavelength of incident X-ray, high flux is necessary to detect weak signals at high Q values. This is because the scattering intensity decreases significantly at higher Q ranges, and a high flux ensures sufficient signal-to-noise ratio for accurate data collection and analysis. Meanwhile, a lower background is essential to acquire high-quality data. Therefore, a well-collimated light source and a thin container with minimal signal interference are necessary to achieve optimal experimental conditions.

The advent of synchrotron-based radiation sources has provided X-rays with high intensity and short wavelengths, enabling the acquisition of accurate and reliable PDF data. To date, a series of beamlines equipped with total scattering techniques have been established, including beamline I15-1 at Diamond Light Source (DLS) [7], beamline Powder Diffraction (PD) at the Australian Synchrotron [8], beamline 28-ID-1 at National Synchrotron Light Source II (NSLS-II) [9], beamline BL04B2 at Super Photon ring-8 (SPring-8) [10], ID11 and ID15A of European Synchrotron Radiation Facility (ESRF) [11, 12]. Notably, the total scattering method was successfully implemented at Shanghai Synchrotron Radiation Facility (SSRF) 13W beamline [13]. Furthermore, the SSRF phase-II beamline project was fully completed in 2023, with the Ultra-hard X-ray Application Beamline providing total scattering capabilities at energies up to 162 keV [14]. Over the past few decades, the total scattering method has been extensively employed in structural studies of liquids (including melts) [15–18], amorphous materials [15, 19], disordered crystalline materials [20, 21] and so on. It is important to emphasize that the pair distribution function (PDF) has played

* Supported by the National Natural Science Foundation of China (No.2020YFA0406101) and Jialin Xie funding of Institute of High Energy Physics, CAS (No.E4546CU210)

† Corresponding author, Xiaodong Li, lixd@ihep.ac.cn

a key role in elucidating local structures, which are fundamentally critical for understanding amorphous and disordered systems.

The Beijing Synchrotron Radiation Facility (BSRF) is a first-generation synchrotron source, featuring an electron storage ring operating at an energy of 2.5 GeV in dedicated mode. BSRF operates in two modes: dedicated mode and parasitic mode. To optimize the use of the parasitic mode, the original biological macromolecule crystallography station was relocated to the 1W2 straight section, while the 3W1 station was transformed into a high-energy beamline facility. In 2019, a superconducting wiggler (SCW) was successfully installed in the 3W1 beamline of BSRF, replacing the original permanent magnetic wiggler. This upgrade provides a broader energy range from 40 keV to 80 keV while delivering sufficiently high flux. These improvements have motivated us to develop a high-energy X-ray total scattering apparatus at the 3W1 beamline. The aim of this study is to report the optimization process of this device and to present benchmark total scattering measurements conducted at this beamline, showcasing the capabilities it offers to our user community.

II. THEORETICAL BASIS

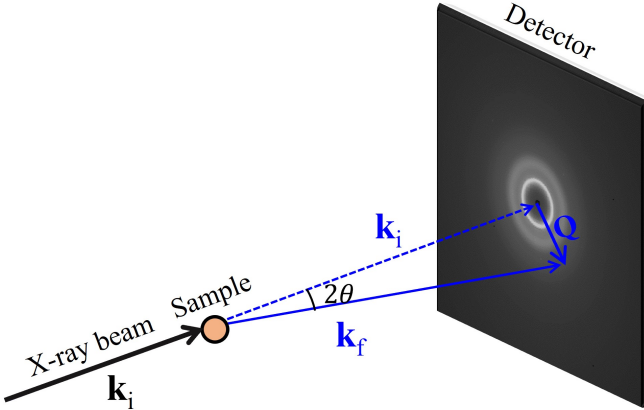


Fig. 1. Scattering triangle of wavevectors of a typical total scattering experiment [22].

The scattering triangle of wavevectors in a typical total scattering experiment is shown in fig.1, where k_i and k_f represent the momentum before scattering and after scattering, respectively. The scattering intensity includes both elastic scattering and inelastic scattering, but elastic scattering plays a major role and determines the diffraction pattern. Here we assume that there was no energy exchange between the incident quantum and sample, such that $k_i = k_f = 2\pi/\lambda$. Q is the scattering vector, $Q = k_i - k_f$, for isotropic samples, $|Q| = Q$. As such, the scattering vector Q is related to the incident wavelength λ and scattering angle 2θ via:

$$|Q| = Q = 2k_i \sin \theta = \frac{4\pi}{\lambda_0} \sin \theta. \quad (1)$$

In a scattering experiment, the structure factor, $S(Q)$, is related to the measured differential scattering cross section, $I(Q)$ [23]:

$$S(Q) - 1 = \frac{I(Q) - (\sum_i c_i f_i^2(Q)) - C(Q)}{[\sum_i c_i f_i(Q)]^2} \quad (2)$$

where c_i is the atomic fraction of element i , $f_i(Q)$ the X-ray atomic form factor, and $C(Q)$ the inelastic (Compton) scattering contribution. The pair distribution function $G(r)$ could be calculated by Fourier transformation of $S(Q)$ via:

$$G(r) - 1 = \frac{1}{2\pi^2 r \rho} \int_{Q_{\min}}^{Q_{\max}} Q[S(Q) - 1] \sin(Qr) dQ \quad (3)$$

where Q_{\min} and Q_{\max} represent the finite range in reciprocal space used during Fourier Transform, which is limited by Q range of the instrument, and ρ is the atomic number density in \AA^3 [24]. Except for $G(r)$, total density function $D(r)$ and total correlation function $T(r)$ is often used in the publications [23], $D(r) = 4\pi\rho r[G(r) - 1]$, $T(r) = 4\pi\rho rG(r)$, peaks in $T(r)$ indicate the existence of atoms with a density exceeding the average number density at a distance r , whereas a valley suggested the absence of atoms.

III. LIGHT SOURCE PARAMETERS

The total scattering method was designed and developed at 3W1 beamline of BSRF. Currently the 3W1 is the only beamline that can provide high energy ($E > 50$ keV) X-ray flux in the BSRF with a 2.3 T super-conducting wiggler. A sagittal focusing monochromator with a Si (111) crystal was placed at 32 meters away from the source. With horizontal focusing of the monochromator, the beam size before beam defining slit (slit 1 in fig.3) is 1.7(H) mm \times 2.9(V) mm. Total photon energy is in the range of 50-70 keV and the energy resolution is better than 0.65%. The beam will be optimized by adjusting bending radius of the second crystal before the total scattering experiment. Calculated photon flux and Q space resolution of 3W1 beamline are shown in fig.2. From fig.2(b), subtle differences for $\Delta Q/Q$ at three energy and a value of $\sim 0.3\%$ at high Q region can meet the requirement of PDF experiment in many cases.

Table 1. Parameters of BSRF 3W1 beamline for total scattering experiment

Animal	Description
Energy (keV)	50-70
Energy resolution	0.65%
Detector	Meru 1717HS, Mar345
Beam size at sample (mm)	0.8×0.8

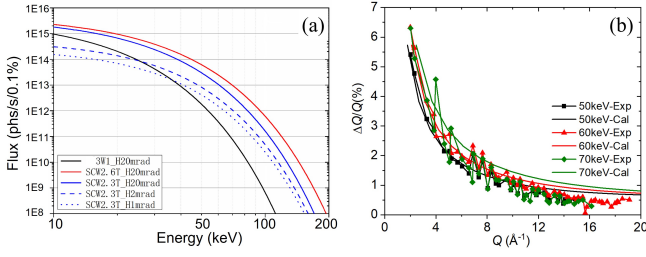


Fig. 2. (a) Calculated photon flux of BSRF 3W1 beamline (blue dashed line); (b) Measured (symbol lines) and calculated (lines) FWHM of selected peaks from the 50 keV, 60 keV and 70 keV total scattering data shown as $\Delta Q/Q$.

IV. APPARATUS OPTIMIZATION PROCESS

A. Experimental setup

High energy X-ray total scattering apparatus were designed and conducted in the range 50-70 keV (wavelengths from 0.247-0.178 Å). Obtaining a clean background is quite important before a total scattering experiment, as the background signal need to be subtracted reliably during data processing. Weak background signal is crucial for weak signal samples, e.g., thin films, nano-materials and other disordered systems. Here we utilized several pairs of slits and an evacuated stainless-steel tube with Kapton windows to decrease parasitic scattering and air scattering. Before the experiment, all of the optics were aligned carefully.

The first set of slit (labeled A in fig.3) close to the incoming beam was used to define the beam size and shape. The beam define slit was composed of four tungsten blades with a thickness of 2 mm and the blades position could be adjusted by high precision slide, thus defining the beam size to 0.5-0.8 mm. Parasitic scattering produced by the beam define slit was unavoidable, so a clean-up slit (C in fig.3) was designed to wipe off the parasitic scattering from slit 1. In the meantime, two lead shields with a thickness of 3 mm were installed just after slit 1 and slit 2 to cut down background radiation. An evacuated stainless-steel tube with a pressure of 10 Torr was designed to reduce the background from air scatter. Another clean up slit (F in fig.3) and a big lead shield were placed just in front of the sample to remove the scatter or diffraction generated by the devices upstream.

At the beginning of the total scattering apparatus design and construction, Mar345 detector was utilized and placed 180 mm downstream of the sample. To increase the experimental efficiency and get a larger Q_{\max} value, we updated the detector to Mercu 1717HS, which is a high speed large two-dimensional flat-panel detector and combines a pixelated detector with a CsI sensor and features 139 μm pitch pixels, 3072×3048 -pixel submodule arrangement, generating a large effective area of 17×17 inches. With Mercu 1717HS, a sample to detector distance of 180 mm and an energy of 60 keV, a Q range of 0.5-25 \AA^{-1} could be obtained. It is worth to mention that benefiting from the high frame rate of Mercu 1717HS (30 fps), it is possible to attempt to collect total scat-

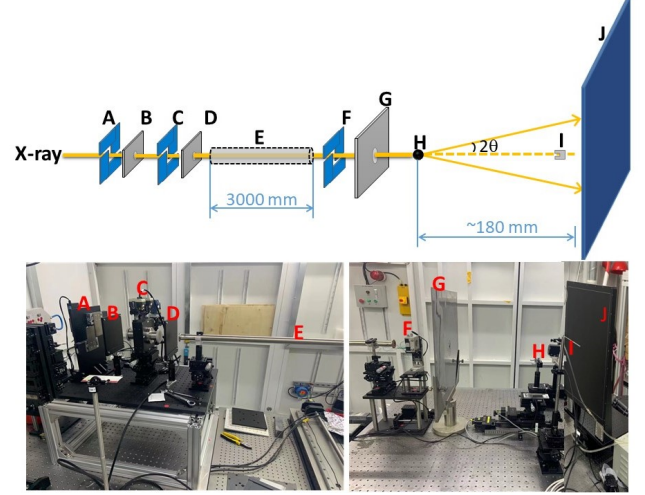


Fig. 3. Schematic layout and Photographs of a typical high-energy scattering set up at 3W1 beamline of BSRF. A: beam define slit (slit 1); B: lead shield 1; C: clean up slit (slit 2); D: lead shield 2; E: evacuated stainless steel tube with mylar windows; F: clean up slit (slit 3); G: lead shield 3; H: sample station; I: beamstop; J: detector

tering and diffraction data up to subseconds, although the data quality might not be good enough due to the low photon flux. XRD pattern of 304 stainless steel during remelting process was collected with a temporal resolution of 0.1 s.

B. Determination of incident X-ray energy

The most important parameter in PDF experiment, Q_{\max} , is limited by the instrument and affected by the energy of the light source. The higher the energy, the larger Q_{\max} value that can be achieved, while the scattering factor of X-ray decreases rapidly with the increase of Q value. To obtain large Q_{\max} and detect the weak signals at high Q region, high energy and high flux are usually required. It can be seen that there is still a high flux at the energy > 50 keV, as shown in fig.2a and the photon flux decreases with the increase of energy. Therefore, the data quality at 50 keV was the first to be tested, and then gradually increase the energy to 60 keV and 70 keV.

Calibration of energy was achieved using a 'two distances method', i.e., (1) adjusting the sagittal monochromator to the target energy; (2) using the standard sample LaB_6 and the distance between detector and sample to calibrate the energy preliminarily; (3) moving the sample station by motor with a known distance; (4) calculating scattering angle 2θ according to the geometrical relation of two position of LaB_6 , and the exact energy by using Bragg equation.

The diffraction patterns of CeO_2 were acquired at three distinct energy points, employing a mar 345 detector with an exposure duration of 60 seconds. The X-ray total structure factor $S(Q)$ and pair distribution functions $G(r)$ are illustrated in fig.4a and fig.4b, respectively. The fitting results of CeO_2 at 60 keV, compared with the standard database reported by

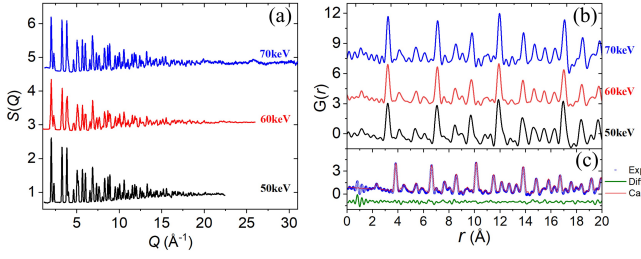


Fig. 4. (a) The X-ray total structure factors $S(Q)$ and (b) pair distribution functions $G(r)$ of CeO_2 at 50 keV, 60 keV and 70 keV with an exposure time of 60 s using a mar345 detector. Note that same Q_{max} of 22 \AA^{-1} was used during the Fourier Transform. (c) Fitting result of CeO_2 at 60 keV with comparison to the standard database reported by Varez et al. [25]

Varez et al [25] were presented in fig.4c. As shown in fig.4c, the peak positions and intensities of $G(r)$ obtained from the BSRF 3W1 beamline aligned well with the standard database, except for the unphysical oscillation in the low r region below 1.5 \AA .

The selection of energy points was determined by comparing the comprehensive data quality. The maximum Q value of instrument at 50 keV, 60 keV and 70 keV is 22, 27 and 32 \AA^{-1} , respectively. From the view of Q_{max} , 70 keV is a good choice. However, in the high Q range, the oscillation of 70 keV is more severe than 50 keV and 60 keV as the flux is lower. From the perspectives of both Q_{max} and the fluctuation of low r region (fig.4b), 60 keV was considered as the target energy for total scattering experiment. The energy could be adjusted at the range of 50-70 keV according to the requirement of users.

V. BENCHMARK RESULTS

A. Ex-situ total scattering experiment of high-entropy perovskite oxides

For ex-situ experiments, samples were collected with Compton tapes and glued to an aluminum alloy frame with an aluminum-tungsten-aluminum ‘sandwich’ configuration, to suppress stray light. The sample station repeatability is controlled at an accuracy of 0.1 mm by changing samples with a magnetic base. Mercu 1717HS detector was placed 200 mm downstream of the sample. The setup was calibrated using the diffraction pattern of polycrystalline CeO_2 powder. The measurement procedure was controlled by iDetector software and 20 s exposure time was set. Background patterns were collected with the same setup and exposure time. The raw diffraction data were reduced from two-dimensional images and corrected for the effects of polarization and geometry using the program Fit2D [26]. The absorption, geometry, detector effect, and the normalization procedure were carried out using PDFgetX3 [27]. As a typical perovskite thermoelectric oxide, SrTiO_3 displays relatively good electrical properties [28]. Total scattering method was utilized to interpret the

structure-property relationship of SrTiO_3 -based oxides with different A-site doping (La, Ba, Ca, and Pb). The X-ray total structure factors $S(Q)$ and pair distribution functions $G(r)$ of SrTiO_3 -based oxides with various A-site doping are shown in fig.5. To explore more detailed structural information, 3D structural models were derived using RMC simulation [29]. The starting configuration consisting of 5000 atoms was created. Several types of constraints were added: the atom-atom approaches, Ti-O connectivity (all titanium atoms were coordinated to certain number oxygen atoms up to 2.5 \AA). The choice of these constraints were determined to avoid physically unrealistic structures. Structural information is derived from counting the atomic configurations generated by RMC simulations.

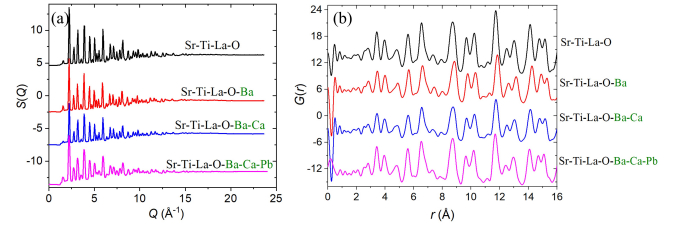


Fig. 5. (a) The X-ray total structure factors $S(Q)$ and (b) pair distribution functions $G(r)$ for SrTiO_3 -based perovskite oxides with various A-site doping collected at 3W1 beamline of BSRF.

From the total scattering experiment and RMC simulation results, A-O and Ti-O bond lengths for SrTiO_3 -based perovskite oxides (ABO_3) of different entropies designed at A sites were extracted to calculate the tolerance factor t via equation $t = \frac{\text{length}(A-O)}{\sqrt{2} \text{length}(B-O)}$. The tolerance factor is a key parameter in perovskite to reflect the correlation between the relative size relationship of elements and structural symmetry, and the extent of the t value deviating from 1 describes the extent of symmetry breaking [30]. In this work, with the t approaching 1, the mobility recovered, meaning that the tolerance factor helps explain why the A-site entropy engineering could enhance the weighted mobility and decouple the carrier-phonon transport by only tuning the average element sizes to tailor the symmetry and Ti displacement, revealing the structural origin of mobility recovery. This work was published in Nature Communications, in cooperation with Qinghua University [31].

B. In-situ heating high energy total scattering experiments

High-temperature experiment is the most common and very important for condensed matter physics and material structure research. For example, the structural response of glasses to temperature and/or pressure is closely pertinent to the ionic transport properties, relaxation, and glass-forming transition. PDF is one of the most effective means to characterize the local order and connectivity of glass, so in-situ heating PDF experiment was used to study the response of different glass structures to temperature. As shown in fig.6a, cou-

pled with high energy synchrotron radiation facility, a high-temperature and high-pressure device was designed with a large exit angle $2\theta > 40^\circ$, with a temperature up to 873 K and pressure to 40 atm (BEIJING OPERANDO TECHNOLOGY CO., LTD).

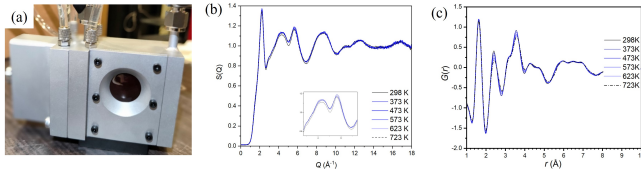


Fig. 6. (a) Photography of the high-temperature and high-pressure device installed at 3W1 beamline, (b) X-ray total structure factors $S(Q)$ and (c) pair distribution functions $G(r)$ of bioactive glasses at different temperatures.

Bioactive glasses are extensively utilized in orthopedics and dentistry. The structural rearrangement upon heating is a key factor in determining its processability. Here, in cooperation with Shanghai Jiao Tong University, we tracked the structural changes of Hench's composition glass [32] using in-situ high energy X-ray total scattering, and the results are presented in fig.6b and 6c. As shown in fig.6b, the first sharp diffraction peak (FSDP) exhibits minimal variation upon heating, indicating that the medium-range order Si-O-Si rings/chains maintain approximate rigidity and cannot be depolymerized by heating below T_g . This subtle change of FSDP is also reminiscent in real-space structural correlations (as depicted by $G(r)$ plot in the (c) panel). The shoulder peak around 3.2 Å remain almost constant, implying that the Si-Si packing is intact, thereby suggesting that these large Si-O-Si rings or chains are rigid. In contrast to FSDP, the second peak in $S(Q)$ patterns undergoes considerable change with an increase in temperature, indicating the nonnegligible rearrangement of short-range order (SRO) local structures upon heating. The changes of the SRO structures can be intuitively visualized in $G(r)$ patterns, as the intensities of peaks at 2.4 Å and 3.6 Å decreased markedly at high-temperature conditions, elucidating that the modifiers-oxygen and modifiers-cations interactions will be much weakened upon heating.

C. Total scattering coupled with Raman spectra and acoustic levitator

X-ray total scattering can realize the atomic scale observation and Raman spectroscopy is sensitive to chemical species in the solution. To obtain the chemical species information and local atomic structural evolution of solutions under low gravity conditions, a multi-mode platform integrating an acoustic levitator, portable Raman spectrometer, and high energy X-ray total scattering was constructed to study the structure of levitated aqueous solutions droplets. The schematic of the multi-mode platform was shown in fig.7a. In the process of experiment, the solutions were injected into a 0.5 mm^3 -2 mm^3 droplet, the X-ray beam and Raman spectrometer was focused on the same droplet simultaneously. Several colored

droplets were shown in the inset of Fig.7b for visual clarity, although the detected solutions are colorless. The scattering and Raman spectra data of aqueous M_2SO_4 ($\text{M} = \text{Li}, \text{Na}, \text{K}$) solutions were shown in fig.7b and 7c, respectively. This method is expected to be used in the study of precious samples (1.0 L) and in-situ observation of chemical reactions in solution. It is noteworthy that, combined with laser heat-

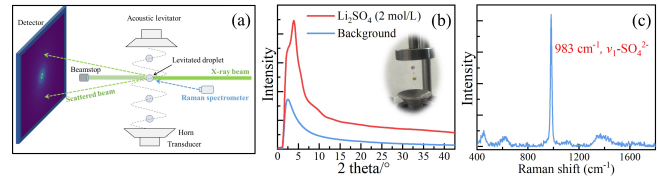


Fig. 7. (a) Schematic of the main components of an acoustic levitator; (b) total scattering patterns with an exposure time of 30 s and (c) Raman spectrum of 2 mol/L Li_2SO_4 aqueous solution droplet, the inset shows several levitated droplets.

ing and temperature-controlled system, the levitation device is applicable for detecting the microstructure of high temperature melts in a container-free environment, eliminating heterogeneous nucleation at the melt-container interface and increasing the propensity for supercooling. A humidity control system is also available, demonstrating the potential accomplishment of in-situ studies on the evaporation and crystallization processes of aqueous droplets. The levitation platform is established in cooperation with Qinghai Institute of Salt Lakes, Chinese Academy of Sciences. More research work is referred to publications by Yongquan Zhou et al [33–35].

D. Total scattering experiment under in-situ magnetic field

In cooperation with Shanghai University, a magnetic field of 2 T (fig.8a) was developed at 3W1 beamline to probe the microstructure of liquid metals under different magnetic fields and explore the influence mechanism of static magnetic field on Ga-based alloys. During the in-situ magnetic field experiment, samples were injected into capillary tubes and loaded between two magnetic poles, and placed at 200 mm upstream of detector. The structural information was collected using a mar345 detector with an exposure time of 400 s. The X-ray total structure factor $S(Q)$ and pair distribution function $G(r)$ of Ga-based alloys at 0 T and 0.5 T was shown in fig.8b. With the addition of magnetic field, subtle changes of $G(r)$ and $S(Q)$ were observed, indicating the weak variation of Ga-based alloys microstructure. This apparatus provides a powerful method to probe the microstructure of liquid metals at various magnetic field intensities.

Apart from total scattering experiment, high energy diffraction experiment coupled with in-situ tensile frame was also conducted with a longer sample-to-detector distance about 800 mm. A Gatan microtension tester equipped with a home-built tensile jig was used for tensile testing. Utilizing the in-situ tensile frame, we investigated the anisotropic phase transition, deformation behaviors, orientation evolution of addi-

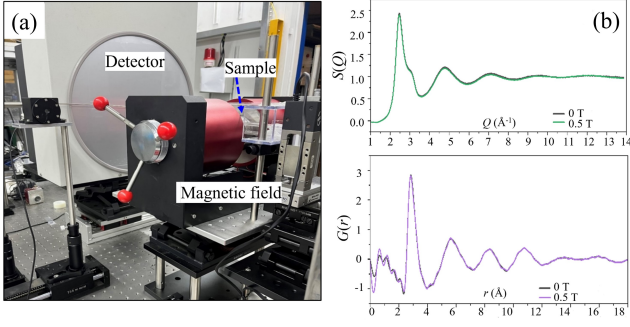


Fig. 8. (a) In-situ magnetic field developed at 3W1 beamline of BSRF; (b) The X-ray total structure factor $S(Q)$ and pair distribution function $G(r)$ of Ga-based alloys at 0 T and 0.5 T.

tively manufactured NiTi alloy during loading, in cooperation with Shanghai University. We refer the reader to relevant publications [36–38], where Pengyue Gao et. al explored the stress-induced phase transformation and lattice correspondence in NiTi shape memory alloy during deformation using in-situ high energy synchrotron X-ray diffraction. In addition, the dislocation density of refractory multi-principal element alloys (MPEAs) under tension was determined according to the Williamson–Hall method, shedding light on the synergistic combination of ultrahigh strength and large tensile ductility in these advanced materials [39–42].

VI. CONCLUSIONS

The high energy X-ray total scattering setups developed at 3W1 beamline of BSRF was described in this paper. Utilizing an energy of 60 keV and a large-area detector, a significant amount of high-quality data was obtained and applied in related research. The apparatus is compatible with various experimental environments, including a magnetic field of 2 T, a custom-designed heating furnace with a temperature range of 293–873 K and a pressure of 40 atm, and a tensile frame capable of applying a maximum tension of 2 kN at temperatures up to 823 K. This work demonstrates that the total scattering apparatus at 3W1 is capable of collecting PDF data with a satisfactory signal-to-noise ratio for amorphous and disordered crystalline materials. It is worth mentioning that beamline scientists at BSRF are currently working on the construction of a new synchrotron light source located in Huairou, Beijing, China.

VII. PERSPECTIVES OF TOTAL SCATTERING TECHNIQUES AT HEPS

High Energy Photon Source, HEPS, the first fourth-generation synchrotron light sources in Asia, will be accom-

plished by the end of 2025. HEPS will accelerate electrons up to energies of 6 GeV and produce high energy beam that can probe samples at nanometer scales. Its time resolution will be 10,000 times better than that achieved by third-generation synchrotrons [43]. There are a couple of beamlines providing total scattering method in HEPS, e.g., Structural Dynamics, Engineering Materials and High Pressure beamlines. Structural Dynamics Beamline (SDB) of HEPS is dedicated to elucidating the dynamic behavior and structural transformations of materials under varying conditions. Benefiting from the dual advantages of high energy and high flux offered by fourth-generation synchrotron light sources, the SDB beamline provides both conventional PDF and time-resolved PDF methods, utilizing a large-area detector and a direct detector with MHz rates, respectively. Additionally, aerodynamic levitation techniques will be combined with the PDF method to study the structure of liquids, melts and pharmaceutical drugs under containerless conditions. Engineering Materials Beamline (EMB) provides high energy X-ray beam with an energy of 100 keV, which is proper to conduct typical PDF experiment with a larger Q_{\max} and better spatial resolution. High Pressure Beamline (HPB) is featured with high pressure experiment, where PDF method can be combined with a high-pressure technique to study the behavior of systems under extreme conditions at monochromatic beam between 20 and 75 keV with a flux of 10^{12} phs/s. It is worth mentioning that both of Engineering Materials and High Pressure Beamlines possess of Eiger2 XE 16M detectors, which will help users collect diffraction data with better signal-to-noise ratio. At High Pressure and Structural Dynamics Beamline, X-ray beam will be focused to micro scale, holding great promise for detecting solid-liquid interfaces structure during the process of crystal growth, electro-catalysis and so on. More information for beamline information of HEPS can be found online at: <https://www.ihep.ac.cn/dkxzz/HEPS/xmgk/HEPSjj/>.

VIII. ACKNOWLEDGEMENTS

This development of total scattering method at BSRF was funded by National Key Basic Research Program of China (grant No. 2020YFA0406101). This work was partially funded by Jialin Xie funding of Institute of High Energy Physics, CAS (No. E4546CU210). The upgrade of 3W1 beamline was supported by Chinese Academy of Sciences major achievements cultivation project (grant No. Y91G714). Dr. Chris Benmore at Advanced Photon Source and Prof. Yang Ren at City University of Hong Kong are thanked for helpful preliminary discussion. We also thank beamline scientists of BSRF 3W1 beamline for kindly help in the high energy X-ray experiment.

- [1] Takeshi Egami, Simon J L Billinge. Underneath the Bragg peaks: Structural Analysis of Complex Materials[Z]. Amsterdam: Elsevier, 2003: 7, 3-404.
- [2] Benmore C J, Gonzalez G B, Alderman O, et al., Hard x-ray methods for studying the structure of amorphous thin films and bulk glassy oxides[J]. *J Phys Condens Matter*, 2021: 33, 19. doi: 10.1088/1361-648X/abe352
- [3] Gao C, Jiang Z, Wang P, et al. Metal-Organic Framework Glass Anode with an Exceptional Cycling-Induced Capacity Enhancement for Lithium Ion Batteries[J]. 2021. doi: 10.26434/CHEMRXIV.14745477.V1
- [4] Alderman O, Wilding M C, Tamalonis A, et al. Iron K-edge X-ray absorption near-edge structure spectroscopy of aerodynamically levitated silicate melts and glasses[J]. *Chemical Geology*. 2017, 453: 169-185. doi:10.1016/j.chemgeo.2017.01.020
- [5] Jian, Wang, Jinglin, et al. In-situ studies on the micro-structure evolution of $A_2W_2O_7$ ($A = Li, Na, K$) during melting by high temperature Raman spectroscopy and density functional theory[J]. *Spectrochimica Acta Part A: Molecular and Biomolecular Spectroscopy*. 2017. doi:10.1016/j.saa.2017.05.046
- [6] Wang, Min, Simon, et al. Quantitative Studies on the Structure of Molten Binary Potassium Molybdates by in Situ Raman Spectroscopy and Quantum Chemistry ab Initio Calculations[J]. *Analytical chemistry*. 2018. doi:10.1021/acs.analchem.8b01470
- [7] Sutter J P, Chater P A, Hillman M R, et al. Three-energy focusing Laue monochromator for the diamond light source x-ray pair distribution function beamline I15-1[J]. *AIP Conference Proceedings*. 2016, 1741(1). doi:10.1063/1.4952877
- [8] D'Angelo A M, Brand H E, Mitchell V D, et al. Total scattering measurements at the Australian Synchrotron Powder Diffraction beamline: capabilities and limitations[J]. *Journal of Synchrotron Radiation*. 2023, 30(2): 327-339. doi:10.1107/S1600577522011614
- [9] Ivashkevych O, Abeykoon M, J. Adams, G. Bischof Hard X-ray pair distribution function (PDF) beamline and END-station control system[Z]. Brookhaven National Lab.(BNL), Upton, NY (United States), 2019. doi:10.18429/JACoW-ICALEPCS2019-THBPP04
- [10] Yamada H, Nakada K, Takemoto M, et al. Fully automated measurement system for temperature-dependent X-ray total scattering at beamline BL04B2 at SPring-8[J]. *Journal of Synchrotron Radiation*. 2022, 29(2): 549-554. doi:10.1107/S1600577521013527
- [11] Bernasconi A, Wright J, Harker N. Total scattering experiments on glass and crystalline materials at the ESRF on the ID11 Beamline[J]. *Powder Diffraction*. 2015, 30(S1): S2-S8. doi:10.1017/s0885715614001304
- [12] Vaughan G B M, Baker R, Barret R, et al. ID15A at the ESRF-a beamline for high speed operando X-ray diffraction, diffraction tomography and total scattering[J]. *Journal of Synchrotron Radiation*. 2020, 27(2): 515-528. doi:10.1107/S1600577519016813
- [13] Xiao-Juan Zhou, Ju-Zhou Tao, Han Guo and He Lin. Atomic pair distribution function method development at the Shanghai Synchrotron Radiation Facility[J]. *Chin. Phys. B*. 2017, 26(7): 076101. doi:10.1088/1674-1056/26/7/076101
- [14] Ren-Zhong Tai, Zhen-Tang Zhao. Overview of SSRF phase-II beamlines[J]. *Nuclear Science and Techniques*. 2024, 35: 137. doi:10.1007/s41365-024-01487-1
- [15] Shi C, Alderman O L, Berman D, et al. The structure of amorphous and deeply supercooled liquid alumina[J]. *Frontiers in Materials*. 2019, 6: 38. doi:10.3389/fmats.2019.00038
- [16] Shi C, Oliver L G A, Tamalonis A, et al. Redox-structure dependence of molten iron oxides[J]. *Communications Materials*. 2020, 80(1): 1-7. doi:10.1038/s43246-020-00080-4
- [17] Shi C, Oliver L G A, Tamalonis A, et al. The structure of molten calcium ferrite under various redox conditions[J]. *Phil. Trans. R. Soc. A*. 2023. doi:10.1098/rsta.2022.0352
- [18] Wilke S K, Benmore C J, Alderman O L G, et al. Plutonium oxide melt structure and covalency[J]. *Nature Materials*. 2024. doi:10.1038/s41563-024-01883-3
- [19] Lan S, Zhu L, Wu Z, et al. A medium-range structure motif linking amorphous and crystalline states[J]. *Nature Materials*. 2021, 20(10): 1347-1352. doi:10.1038/s41563-021-01011-5
- [20] Billinge S J L. The rise of the X-ray atomic pair distribution function method: a series of fortunate events[J]. *Philosophical transactions of the Royal Society of London. Series A: Mathematical, physical, and engineering sciences*. 2019, 377(2147): 20180413. doi:10.1098/rsta.2018.0413
- [21] Bridges F, Keiber T, Juhas P, et al. Local vibrations and negative thermal expansion in ZrW_2O_8 [J]. *Phys Rev Lett*. 2014, 112(4): 45505. doi:10.1103/PhysRevLett.112.045505
- [22] Fischer H E, Barnes A C, Salmon P S. Neutron and x-ray diffraction studies of liquids and glasses[J]. *Reports on Progress in Physics*. 2006, 69(1): 233. doi:10.1088/0034-4885/69/1/R05
- [23] Keen D A. A comparison of various commonly used correlation functions for describing total scattering[J]. *Journal of Applied Crystallography*. 2001, 34(2): 172-177. doi:10.1107/S0021889800019993
- [24] Benmore C J. A review of high-energy X-ray diffraction from glasses and liquids[J]. *ISRN Materials Science*. 2012, 2012. doi:10.5402/2012/852905
- [25] Varez, A.; Garcia-Gonzalez, E.; Jolly, J.; Sanz, J. Structural characterization of $Ce_{1-x}Zr_xO_2$ ($0 \leq x \leq 1$) samples prepared at 1650 C by solid state reaction. A combined TEM and XRD study[J]. *Journal of the European Ceramic Society*. 2007, 27: 3677-3682. doi:10.1016/j.jeurceramsoc.2007.02.014
- [26] Hammersley A P, Svensson S O, Hanfland M, et al. Two-dimensional detector software: from real detector to idealised image or two-theta scan[J]. *International Journal of High Pressure Research*. 1996, 14(4-6): 235-248. doi:10.1080/08957959608201408
- [27] Juhas P, Davis T, Farrow C L, et al. PDFgetX3: A rapid and highly automatable program for processing powder diffraction data into total scattering pair distribution functions[J]. *J. Appl. Cryst*. 2013(46): 560-566. doi:10.1107/S0021889813005190
- [28] Wang J, Zhang B, Kang H, et al. Record high thermoelectric performance in bulk-SrTiO₃ via nano-scale modulation doping[J]. *Nano Energy*. 2017(35): 387-395. doi:10.1016/j.nanoen.2017.04.003
- [29] McGreevy R L. Reverse monte carlo modelling[J]. *Journal of Physics: Condensed Matter*. 2001, 13(46): R877. doi:10.1088/0953-8984/13/46/201
- [30] Tilley R J D. *Perovskites: Structure-Property Relationships*[J]. John Wiley Sons. 2016. doi:10.1557/mrs.2017.81
- [31] Zheng Y, Zhang Q, Shi C, et al. Carrier-phonon decoupling in perovskite thermoelectrics via entropy engineering[J]. *Nature Communications*. 2024, 15(15): 1-12. doi:10.1038/s41467-024-52063-5

- [32] Cao W, Hench L L. Bioactive Materials[J]. *Ceramics International*. 1995, 22: 493-507. doi:10.1016/j.ceramint.1995.00126-3
- [33] Wang G, Ohara M B K, Ohara K, et al. Hydration of Alkali Metal and Halide Ions from Static and Dynamic Viewpoints[J]. *Journal of physical chemistry letters*. 2023. doi:10.1021/acs.jpclett.3c01302
- [34] Zhou Y, Yamaguchi T, Ikeda K, et al. Dihydrogen Bonds in Aqueous NaBD4 Solution by Neutron and X-ray Diffraction[J]. *Journal of Physical Chemistry Letters*. 2020, 11(5): 1622-1628. doi:10.1021/acs.jpclett.9b03183
- [35] Jing Z, Yamaguchi T, Ohara K. Alkali Metal Ion Recognition by 18-Crown-6 in Aqueous Solutions: Evidence from Local Structures[J]. *The journal of physical chemistry, B. Condensed matter, materials, surfaces, interfaces biophysical*. 2023, 127(21): 4858-4869. doi:10.1021/acs.jpcb.3c01875
- [36] Gao P, Li R, Shi C, et al. Revealing the orientation preference along with localized Lüders-type deformation in polycrystalline NiTi SMA by in-situ synchrotron-based high energy X-ray diffraction[J]. *Vacuum*. 2024, 221: 112921. doi:10.1016/j.vacuum.2023.112921
- [37] Gao P, Li R, He D, et al. Understanding the asymmetric orientations and stress states in polycrystalline NiTi SMA by in-situ synchrotron-based high-energy X-ray diffraction[J]. *Materials Science and Engineering: A*. 2024, 896: 146301. doi:10.1016/j.msea.2024.146301
- [38] Gao P, Zhang Z, Huang J, et al. In-situ synchrotron diffraction study on the anisotropic deformation and phase transformation behaviors in NiTi shape memory alloy fabricated by laser powder bed fusion[J]. *Additive Manufacturing*. 2024, 96: 104566. doi:10.1016/j.addma.2024.104566
- [39] An Z, Li A, Mao S, et al. Negative mixing enthalpy solid solutions deliver high strength and ductility[J]. *Nature*. 2024, 625(7996): 697-702. doi:10.1038/s41586-023-06894-9
- [40] An Z, Mao S, Liu Y, et al. Inherent and multiple strain hardening imparting synergistic ultrahigh strength and ductility in a low stacking faulted heterogeneous high-entropy alloy[J]. *Acta Materialia*. 2023, 243: 118516. doi:10.1016/j.actamat.2022.118516
- [41] An Z, Yang T, Shi C, et al. Negative enthalpy alloys and local chemical ordering: a concept and route leading to synergy of strength and ductility[J]. *National Science Review*. 2024, 11: e26. doi:10.1093/nsr/nwae026
- [42] An Z, Mao S, Vayyala A, et al. Multiscale hierarchical heterostructure yields combined high strength and excellent ductility in a Co-Cr-Fe-Ni-Al negative enthalpy alloy[J]. *Acta Materialia*. 2024, 281: 120366. doi:10.1016/j.actamat.2024.120366
- [43] Conroy G. World's brightest X-rays: CHINA IS FIRST IN ASIA TO BUILD NEXT-GENERATION SYNCHROTRON[J]. *Nature*. 2024, 629: 740. doi:10.1038/d41586-024-01346-4